Performance Analysis of a Near-Field Thermophotovoltaic Device With a Metallodielectric Selective Emitter and Electrical Contacts for the Photovoltaic Cell

Yue Yang
School for Engineering of Matter, Transport, and Energy, Arizona State University, Tempe, AZ 85287

Jui-Yung Chang
School for Engineering of Matter, Transport, and Energy, Arizona State University, Tempe, AZ 85287

Payam Sabbaghi
School for Engineering of Matter, Transport, and Energy, Arizona State University, Tempe, AZ 85287

Liping Wang[1]
School for Engineering of Matter, Transport, and Energy, Arizona State University, Tempe, AZ 85287
e-mail: liping.wang@asu.edu

The photon transport and energy conversion of a near-field thermophotovoltaic (TPV) system with a selective emitter composed of alternate tungsten and alumina layers and a photovoltaic cell sandwiched by electrical contacts are theoretically investigated in this paper. Fluctuational electrodynamics along with the dyadic Green's function for a multilayered structure is applied to calculate the spectral heat flux, and the photocurrent generation and electrical power output are solved from the photon-coupled charge transport equations. The tungsten and alumina layer thicknesses are optimized to obtain maximum electrical power output for bare TPV cell. The spectral heat flux is much enhanced when plain tungsten emitter is replaced with the multilayer emitter due to the effective medium intrinsic lossy property and additional surface plasmon polariton coupling in the tungsten thin film, for which the invalidity of effective medium theory to predict photon transport in the near field with multilayer emitters is discussed. Effects of a gold back reflector and indium tin oxide front coating with nanometer thickness, which could practically act as the electrodes to collect the photon-generated charges on the TPV cell, are explored. The conversion efficiency of 23.7% and electrical power output of 0.31 MW/m^2 can be achieved at a vacuum gap distance of 100 nm when the emitter and receiver temperature are, respectively, set as 2000 K and 300 K. [DOI: 10.1115/1.4034839]

Keywords: near-field radiation, thermophotovoltaic, fluctuational electrodynamics, multilayer emitter

1 Introduction

Thermophotovoltaic (TPV) energy conversion system, which consists of two main components of thermal emitter and TPV cell, is a direct energy conversion process from heat to electricity through electron–hole pair generation from absorbed thermal radiation. The advantages of TPV systems including versatile thermal sources, high power output and conversion efficiency potential [1], and no moving parts, make it possible for space, civilian, industrial, military, and microelectronics applications. However, one of the major challenges for current TPV systems is the low power output and conversion efficiency.

Recently, it has been demonstrated that the radiative heat transfer in near field can be greatly enhanced to exceed the blackbody limit for a few orders of magnitude due to the resonant coupling of evanescent waves [2–6]. The near-field radiation was proposed by Whale and Cravalho [7] to improve the power output of TPV systems, in which the blackbody emitter and extra recombination loss were considered. Laroche et al. [8] also developed a model of near-field TPV considering a tungsten emitter with TPV cell of 100% quantum efficiency. Basu et al. [1] conducted a review on the near-field TPV systems in 2007, and Park et al. [9] analyzed a near-field TPV system with plain tungsten thermal emitter, and with the consideration of energy absorption and charge transport in different regions of the TPV cell. Later, Francoeur et al. [10] investigated the thermal impacts on the performance of near-field TPV system by solving the coupled near-field thermal radiation, charge transport, and heat transport formulations in TPV cell, and concluded that the cell temperature will greatly affect the TPV performance. Bright et al. [11] studied the effect of a gold reflector added at the cell backside, which leads to enhanced conversion efficiency by reflecting the useless long-wavelength energy back to emitter.

On the other hand, efforts have been made to design selective emitters for far-field TPV systems to improve the conversion efficiency. Due to the narrowband radiation, rare-earth oxides were the earliest selective emitters [12,13]. Benefiting from the improvement of micro/nanoscale fabrication technique, micro/nanostructured surfaces were also used to achieve the selective emission. The grating structures with different dimensions were considered as the most widely applicable selective emitters and filters [14–16]. Magnetic polaritons, which account for the strong coupling of external electromagnetic waves with the magnetic resonance excited inside the nanostructure, is another mechanism used to achieve selective emission [17–19]. Recently, the metamaterials using epsilon-near-zero (ENZ) or epsilon-near-pole (ENP) have also been proposed as the selective emitter [20]. Narayanaswamy and Chen [21] showed that a stack of alternate tungsten and alumina layers could be applied as the selective emitter of far-field TPV systems.

One question is whether the emission spectrum can be spectrally tuned to enhance the conversion efficiency for near-field

[1]Corresponding author.

Presented at the 2016 ASME 5th Micro/Nanoscale Heat & Mass Transfer International Conference. Paper No. MNHMT2016-6471.

Contributed by the Heat Transfer Division of ASME for publication in the Journal of Heat Transfer. Manuscript received October 9, 2015; final manuscript received June 20, 2016; published online February 7, 2017. Assoc. Editor: Zhuomin Zhang.

TPV systems. Narayanaswamy and Chen [22] presented the idea to improve the performance of near-field TPV by exciting SPhP coupling between the dielectric emitter and optimized TPV cell. Recently, several groups have proposed to coat graphene sheet either on the emitter or on the TPV cell to enhance near-field photon tunneling and thereby higher conversion efficiencies [23,24]. Thin-film germanium emitter as "thermal well" was also demonstrated to achieve spectrally enhanced near-field radiative heat flux with quantized modes [25]. The Drude radiator, which supports surface polaritons in near infrared region, was also considered as the emitter of near field TPV system for achieving quasi-monochromatic radiative heat flux [26]. Tungsten nanowire-based hyperbolic metamaterial emitters were also studied to improve the near-field TPV performance with supported hyperbolic modes [27].

In this study, we theoretically analyze a near-field TPV system consisting of a multilayer emitter with alternate tungsten and alumina layers and a TPV cell made of $In_{0.18}Ga_{0.82}Sb$ sandwiched by front and back electrical contacts. Optical properties of both tungsten and alumina are obtained from Palik's data [28], while $In_{0.18}Ga_{0.82}Sb$, which is an alloy of InSb and GaSb, has a bandgap of $E_g = 0.56$ eV, or equivalently $\lambda_g = 2.22\ \mu$m [28,29]. The dielectric function for $In_{0.18}Ga_{0.82}Sb$ is obtained by interpolating the parameters of materials InSb and GaSb [29]. Although the effect of dopant concentration is not considered in this model, it is still accurate enough to get the consistent results with the experimental measurements [29]. As depicted in Fig. 1, tungsten is set as the first layer of emitter, while the temperatures of the emitter and the TPV cell are set as 2000 K and 300 K, respectively. Although the temperature gradient in TPV cell has been considered before [10], according to the conclusion obtained from Ref. [10], with plain tungsten emitter temperature of 2000 K and a vacuum gap distance of 20 nm, the maximum temperature difference was only 0.5 K, which is negligible to affect TPV cell optical properties. Therefore, it is still reasonable to assume the TPV cell temperature as a uniform value of 300 K in this study. The near-field radiative flux between the multilayer emitter and the TPV cell is calculated, and the mechanisms on the radiative transport will be investigated. The TPV system power output and conversion efficiency will be calculated by solving the charge transport equations. Finally, effects of front and back electrodes, i.e., indium tin oxide (ITO) thin film with nanometer thickness and a gold reflector, will be studied on the photon transport and conversion performance.

2 Theoretical Background

2.1 Near-Field Radiative Transport Between Isotropic Nonmagnetic Multilayer Structures. The fluctuational electrodynamics theory along with the dyadic Green's function for a multilayered structure is applied to calculate the near-field radiative (NFR) heat flux between the emitter and TPV cell. The electric field **E** and magnetic field **H** can be expressed as follows [30]:

$$\mathbf{E}(\mathbf{x},\omega) = i\omega\mu_0 = \int_V \bar{\bar{\mathbf{G}}}_e(\mathbf{x},x',\omega)\cdot\mathbf{j}(x',\omega)dx' \tag{1a}$$

$$\mathbf{H}(\mathbf{x},\omega) = \int_V \nabla\times\bar{\bar{\mathbf{G}}}_e(\mathbf{x},x',\omega)\cdot\mathbf{j}(x',\omega)dx' \tag{1b}$$

where μ_0 is the magnetic permeability in vacuum, and i is the unit of purely imaginary number. $\bar{\bar{\mathbf{G}}}_e(\mathbf{x},x',\omega)$ is the electric dyadic Green's function, which presents the relationship between the electric field $\mathbf{E}(\mathbf{x},\omega)$ at location $\mathbf{x}$ and the space- and time-dependent electric current density $\mathbf{j}(x',\omega)$ at location x' due to thermal fluctuation of charges or dipoles. The expressions of electric dyadic Green's function for a multilayered structure have been well derived [9,21,31–35]. The spectral heat flux at location $\mathbf{x}$ can be expressed as the time-averaged Poynting vector

$$\mathbf{S}_\omega(\mathbf{x},\omega) = \frac{1}{2}\left\langle \mathrm{Re}\left[\mathbf{E}(\mathbf{x},\omega)\times\mathbf{H}^*(\mathbf{x},\omega)\right]\right\rangle \tag{2}$$

where the superscript * denotes the conjugate of complex number.

Therefore, the total radiative flux at the depth of z_m inside the TPV cell can be obtained by integrating the spectral heat flux

$$q''(z_l) = \int_0^\infty S_{z,\omega}(Z_m,\omega)d\omega \tag{3}$$

Then, the energy absorbed by a layer is calculated as the difference between the total heat fluxes at upper and lower interfaces.

2.2 Charge Transport in the TPV Cells. Here, the photocurrent generation is considered separately in different regions of a TPV cell with charge transport equations. The TPV cell is separated into N layers, and with the spectral heat flux absorbed in lth layer with thickness of d_l, denoted as $Q_{\lambda,l}$, the electron–hole pairs generation rate in this layer is described as [9]

$$g_l(\lambda) = \frac{Q_{\lambda,l}}{d_l(hc_0/\lambda)} \text{ with } \frac{hc_0}{\lambda} \geq E_g \tag{4}$$

where h is the Planck constant, c_0 is the light velocity in vacuum, and hc_0/λ is the photon energy at wavelength λ. E_g is the bandgap of TPV cell. This equation indicates that only the photons with energy higher than E_g can generate electron–hole pairs. d_l is the thickness of the lth layer in the receiver.

In depletion region of the TPV cell, the generated electron–hole pairs can be completely collected due to the built-in voltage, and the drift current is expressed as

$$J_{dp}(\lambda) = eg_{dp}(\lambda)L_{dp} \tag{5}$$

where e is the electron charge, and L_{dp} is the depletion region thickness.

On the other hand, minority carrier concentration at p- and n-regions should be calculated to obtain the photocurrent. The electron concentration in p-region can be expressed with the following 1D, steady-state continuity equation [9]:

$$D_e\frac{d^2n_e}{dz^2} - \frac{n_e - n_e^0}{\tau_e} + g(z,\lambda) = 0 \tag{6}$$

The boundary conditions can be set as

$$D_e\frac{dn_e}{dz}\bigg|_{z=0} = u_p\left[n_e(0) - n_e^0\right] \text{ and } n_e|_{z=a} = n_e^0 \tag{7}$$

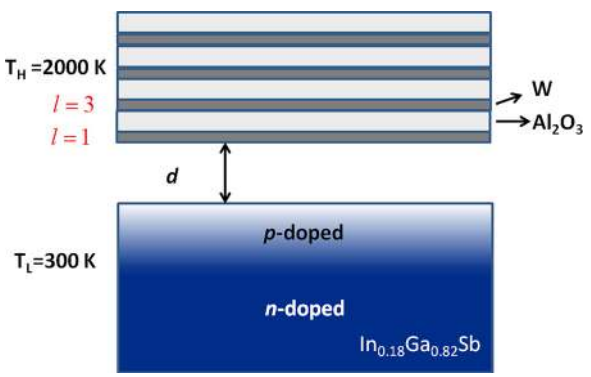

Fig. 1 The configuration of near-field TPV system when applying the multilayer emitter with alternate tungsten and alumina layer, and tungsten is the topmost layer. The TPV cell is made of the alloy $In_{0.18}Ga_{0.82}Sb$. The emitter and cell temperatures are set as 2000 K and 300 K, respectively.

where D_e is the electron diffusion constant, n_e is the local electron concentration, n_e^0 is the equilibrium electron concentration, and τ_e is the electron relaxation time. u_p is the surface recombination velocity in the p-region. The photocurrent generated in the p-region can be then given as

$$J_e(\lambda) = eD_e \frac{dn_e}{dz}|_{z=a} \tag{8}$$

Note that the photocurrent in the n-region, $J_h(\lambda)$ can be obtained in the same way by just replacing the electron in the p-region with hole in the n-region.

For the TPV cell, the same parameters were used with Ref. [9]. The thicknesses of the p-region, depletion region, and n-region are set as 0.4 μm, 0.1 μm, and 10 μm, respectively. The p-region has a doping concentration of $10^{19}\,\text{cm}^{-3}$, and that for n-region is $10^{17}\,\text{cm}^{-3}$. The diffusion coefficient and relaxation time for electron in p-region are set as 125 cm^2/s and 9.75 ns, respectively, while those for hole in n-region are set as 31.3 cm^2/s and 30.8 ns, respectively. The surface recombination velocities on the top surface of p-region and the bottom surface of n-region are set as 7.4×10^4 m/s and 0 m/s, respectively. Recombination on the bottom surface of n-region is not considered because the thickness of n-region is much larger than the hole diffusion length.

The total generated drift current $J_\lambda(\lambda)$ is the summation of the three drift currents $J_\lambda(\lambda) = J_{dp}(\lambda) + J_e(\lambda) + J_h(\lambda)$. The quantum efficiency $\eta_q(\lambda)$, which is the ratio of the number of generated electron–hole pairs and the number of absorbed photons, can be obtained through the total generated drift current and absorbed spectral heat flux [9].

$$\eta_q(\lambda) = \frac{J_\lambda/e}{S_\lambda/(hc/\lambda)} \tag{9}$$

where S_λ is the spectral heat flux absorbed by the whole TPV cell.

The electrical power output can be expressed as [9]

$$P_E = J_{ph}V_{oc}(1 - 1/y)[1 - \ln(y)/y] \tag{10}$$

where $y = \ln(J_{ph}/J_o)$. J_{ph}, V_{oc}, and J_o are, respectively, photocurrent, open circuit voltage, and dark current, whose expressions are obtained from Ref. [9]. The conversion efficiency η, which characterizes the performance of TPV systems, is expressed as the ratio of electrical power output and radiative power input

$$\eta = P_E/P_R \tag{11}$$

where $P_R = \int_0^\lambda S_\lambda d\lambda$ is the total absorbed radiative power by the cell and electrical contacts.

3 Results and Discussions

3.1 Spectral Heat Flux Between the Multilayer Emitter and the TPV Cell Without Electrical Contacts. In order to be considered as semi-infinite, a minimum of 20 layers with alternating tungsten and alumina needs to be considered for the multilayer emitter, which leads to a relative difference in the total heat flux smaller than 1% compared to that with 40 layers. The spectral heat fluxes between the multilayer emitter and the TPV cell with different tungsten and alumina layer thickness are presented in Fig. 2(*a*) at vacuum gap distance of $d = 100$ nm. The tungsten layer thickness is fixed at $t_W = 10$ nm, and the alumina layer thickness varies from 100 nm to 400 nm. The spectral heat flux between the plain tungsten emitter and the TPV cell indicated by the black dash line is also plotted for comparison. It can be clearly seen that the spectral heat flux is much enhanced when the plain tungsten emitter is replaced by the multilayer emitter. As a good selective TPV emitter, it should emit most energy above the bandgap E_g (i.e., wavelengths smaller than $\lambda_g = 2.22\,\mu$m), and little energy below the bandgap to maximize both the power output and conversion efficiency. In order to optimize both the tungsten and alumina layer thicknesses, the electrical power output calculated by Eq. (10) was plotted in Fig. 2(*b*) with different tungsten and alumina layer thickness combinations. The reason to use electrical power output instead of conversion efficiency as the optimal function is because of that after adding the gold reflector layer later, the spectral heat flux below the bandgap will be significantly reduced. Therefore, we care more about the energy above the bandgap between the multilayer emitter and the bare TPV cell, which corresponds to the electrical power output. After comparing all the tungsten and alumina layer thickness combinations shown in Fig. 2(*b*), the optimized value of $t_W = 10$ nm and $t_{Al_2O_3} = 300$ nm is chosen to maximize the electrical power output. Note that all the results shown about the multilayer emitter in the following paragraphs are based on these geometric dimensions.

3.2 Comparison With Effective Medium Theory (EMT). Using the Maxwell–Garnett EMT [36,37], the multilayer emitter can be approximated as a homogeneous and uniaxial medium with components of dielectric function parallel ($\varepsilon_\parallel$) and vertical ($\varepsilon_\perp$) to the surface expressed as follows:

$$\varepsilon_\parallel = f\varepsilon_m + (1 - f)\varepsilon_d \tag{12a}$$

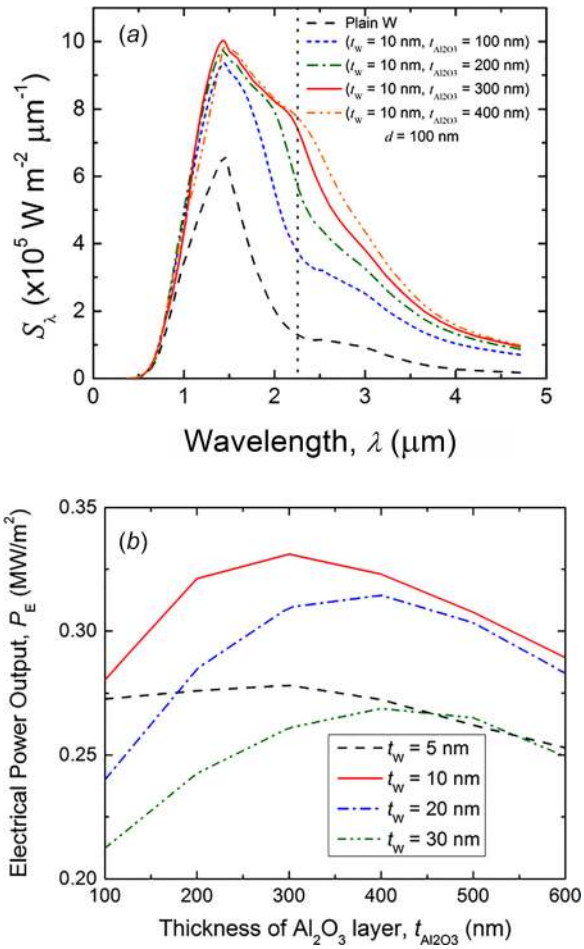

Fig. 2 (*a*) Spectral heat fluxes between the multilayer emitter and the receiver when the tungsten layer thickness is set as 10 nm, while the alumina layer thickness is varied. The dash vertical line indicates the bandgap of TPV cell. (*b*) The electrical power output as a function of alumina layer thickness with different values of tungsten layer thickness. The vacuum gap distance *d* is 100 nm.

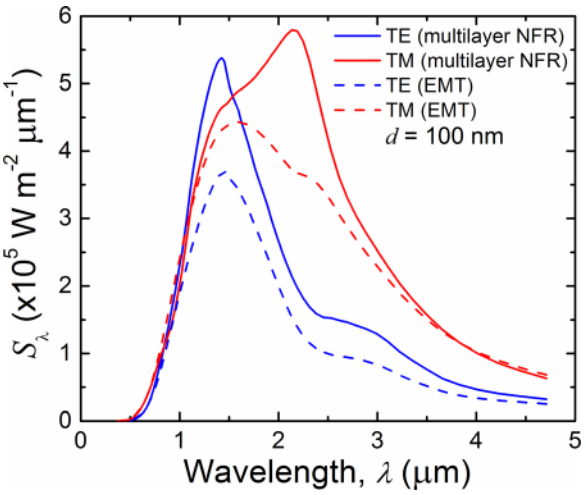

Fig. 3 Comparison of the spectral heat fluxes between the TPV cell and multilayer emitter using exact multilayer NFR calculation and EMT calculation in different polarizations of TE waves and TM waves. The vacuum gap distance is 100 nm.

$$\varepsilon_\perp = \frac{\varepsilon_m \varepsilon_d}{f\varepsilon_d + (1-f)\varepsilon_m} \tag{12b}$$

where f is the volume fraction of metal in the whole structure, and ε_m and ε_d are the dielectric functions of metal (tungsten) and dielectric (alumina) medium, respectively. In order to understand the mechanism that results in the heat transfer enhancement, the spectral heat fluxes are separated into different polarizations, and comparison between the spectral heat fluxes calculated from multilayer NFR and EMT is investigated in Fig. 3. Here, the fluctuational electrodynamics along with wave propagation in anisotropic medium [38] is used to calculate the near-field radiative heat fluxes between the homogeneous uniaxial emitter with effective dielectric functions defined in Eq. (12), and the TPV cell without electrical contacts.

As can be seen from Fig. 3, there is a large deviation between the spectral heat fluxes obtained using EMT and multilayer NFR for TE waves. Note that the basic condition to use EMT is that the characteristic wavelength should be at least 20 times larger than the structure size. However, the characteristic wavelength, which is around 1.5 μm from Fig. 2, is only about five times of the period of multilayer, which is 310 nm. The small ratio between characteristic wavelength and the multilayer structure period results in the invalidity of EMT to predict heat transfer for TE waves. In addition, from the later discussion, we know that the first tungsten layer will contribute most of the energy transfer. The EMT method actually makes a dilute tungsten layer according to Eq. (12*a*), which is only used for TE waves calculation. This also explains the reason why EMT prediction has a lower spectral heat flux than the exact multilayer calculation. One the other hand, when it comes to TM waves, the most significant deviation between the spectral heat fluxes obtained from exact multilayer NFR and EMT is around $\lambda_{SPP} = 2\,\mu$m, where there is a high peak of heat flux from the multilayer NFR calculation that cannot be observed from EMT prediction. The spectral heat flux peak at around $\lambda_{SPP} = 2\,\mu$m for TM waves is caused by the surface plasmon polaritons (SPP) coupling within the tungsten thin film, which will be verified later. This also proves that EMT cannot predict SPP coupling among multilayer structure at small vacuum gap. The invalidity of EMT for multilayer structures in the presence of surface waves has been discussed previously by Ref. [37]. It was shown that the different topmost layer can result in different density of states above the multilayer structure, which cannot be captured by EMT. The effects of finite number of multilayer stacks, defects, and surface roughness during practical fabrication process on the accuracy of EMT prediction were investigated as well [39]. Moreover, Zhang's group quantitatively presented the application condition of EMT to predict the near-field radiative heat transfer between the multilayer structure recently [40]. Note that besides the spectral heat flux peak at round $\lambda_{SPP} = 2\,\mu$m for exact multilayer calculation, another small one at round 2.5 μm can also be observed for EMT method at TM waves.

3.3 Elucidating the Mechanisms for Spectral Near-Field Radiation. In order to elucidate the difference of spectral heat flux between exact multilayer calculation and EMT method for both TE and TM waves shown in Fig. 3, the contour plot of energy transmission coefficient for both TM and TE waves (ξ) between the multilayer emitter and receiver is presented in Fig. 4 using both multilayer NFR calculation and EMT method. The energy transmission coefficient, which only considers the material properties of emitter and receiver, is a function of both angular frequency ω and parallel wavevector β [41]. The relationship between spectral heat flux (S_ω) and transmission coefficient (ξ) can be expressed as

$$S_\omega = \frac{1}{4\pi^2}[\theta(T_H,\omega) - \theta(T_L,\omega)]\int_0^\infty \beta\xi(\omega,\beta)d\beta \tag{13}$$

Note that $\Theta(\omega,T) = \hbar\omega/[\exp(\hbar\omega/k_B T) - 1]$ is the mean energy of a Planck oscillator at thermal equilibrium temperature T, where $\hbar$ and k_B are the Planck constant divided by 2π and the Boltzmann constant, respectively.

Comparing the contour plots in Figs. 4(*a*) and 4(*c*) at TM waves for exact multilayer calculation and EMT method, respectively, the energy transmission coefficients are quite similar except the two different enhancement bands at small angular frequency. The similar behavior of transmission coefficient between these two methods indicate that the spectral heat flux enhancement compared to plain tungsten emitter shown in Fig. 2(*a*) mainly comes from the intrinsic lossy properties of the effective medium. Note that the energy transmission coefficient enhancement at $\omega = 9\times10^{14}$ rad/s in Fig. 4(*a*) exactly corresponds to the heat flux peak at $\lambda_{SPP} = 2\,\mu$m shown in Fig. 3. The coupled SPP dispersion curve for TM waves within the tungsten thin film with vacuum substrate on one side and alumina substrate on the other side is also plotted in Fig. 4(*a*) based on the condition below [42]:

$$\tanh(ik_{2z}t_2)\left(\frac{k_{2z}^2}{\varepsilon_2^2} + \frac{k_{1z}k_{3z}}{\varepsilon_1\varepsilon_3}\right) = \frac{k_{2z}}{\varepsilon_2}\left(\frac{k_{1z}}{\varepsilon_1} + \frac{k_{3z}}{\varepsilon_3}\right) \tag{14}$$

where the subscripts 1, 2, and 3 denote the vacuum substrate, tungsten thin film, and alumina substrate, respectively. $k_{jz} = \sqrt{\varepsilon_j\omega^2/{c_0}^2 - \beta^2}$ ($j = 1, 2, 3$) is the component of wavevector vertical to the interface, and t_2 is the thickness of the tungsten thin film. The excellent match between the coupled SPP dispersion curve and the energy transmission coefficient enhancement for TM waves in Fig. 4(*a*) confirms that the spectral heat flux enhancement with the multilayer emitter results from the SPP coupling within the tungsten thin film. On the other hand, the enhancement band at small angular frequency calculated by the EMT method in Fig. 4(*c*), which corresponds to the spectral heat flux enhancement around 2.5 μm shown in Fig. 3 for TM waves calculated by EMT method, actually results from the hyperbolic modes of the effective medium. Although it is not presented here, the real parts of the parallel and vertical dielectric function components predicted by Eq. (12) have different signs below the angular frequency represented by the blue dash line shown in Fig. 4(*c*). For TE waves illustrated in Figs. 4(*b*) and 4(*d*), these two methods give almost the same behavior of transmission coefficient but

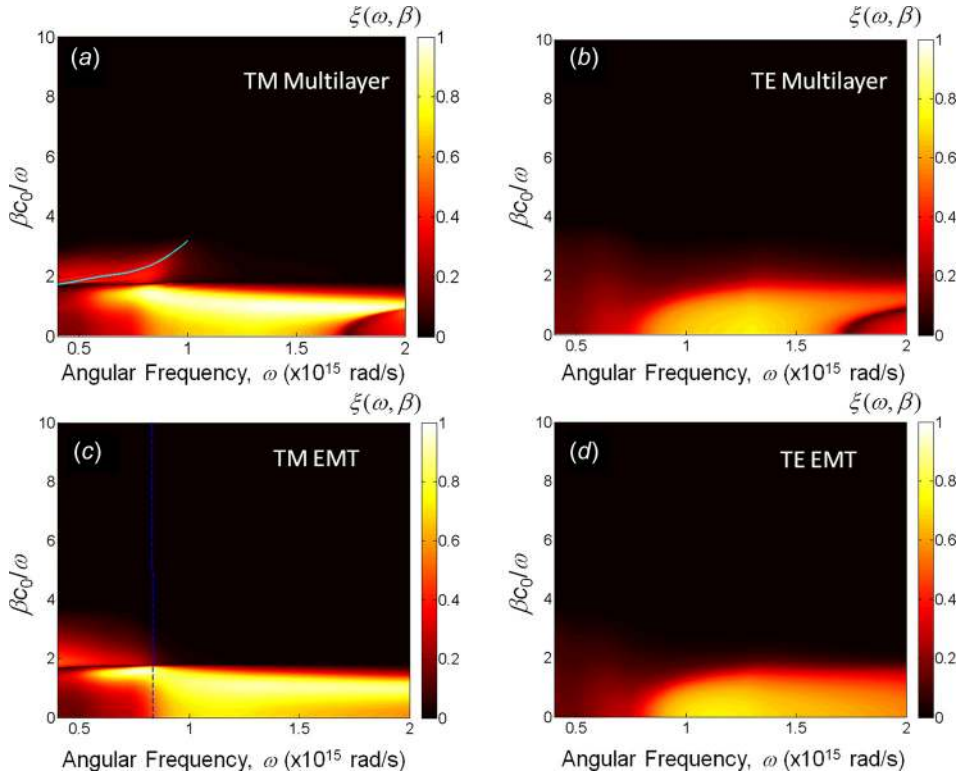

Fig. 4 The contour plots of energy transmission coefficient between multilayer emitter and TPV cell for (*a*) TM and (*b*) TE waves using exact multilayer NFR calculation, and (*c*) TM and (*d*) TE waves using EMT calculation. The dispersion curve within tungsten thin film with substrates of vacuum and alumina on each side is also plotted in (*a*). The blue dash line in (*c*) indicates the transition frequency, below which the parallel and vertical dielectric function components of the effective medium calculated by Eq. (12) have different signs for the real part. Note that the parallel wavevector is normalized to the wavevector in vacuum. The vacuum gap distance is 100 nm.

different amplitudes, for which the EMT method predicts a weaker one due to the reason of a dilute tungsten layer mentioned above.

In order to understand the contribution of emission from each tungsten layer, the spectral heat flux with contributions of both TE and TM waves from different layer of the emitter is plotted in Fig. 5. The first layer of the emitter is the bottom tungsten film as depicted in Fig. 1. From Fig. 5, it can be observed that the spectral heat flux from the bottom tungsten layer is much higher than the other layers, because waves decay very fast into the multilayer emitter, especially for exponentially decayed evanescent waves. The spectral heat flux peak around $\lambda_{ba} = 1.5\,\mu$m at each tungsten layer is due to the band absorption of tungsten, which occurs at both TE and TM waves, while the peak around $\lambda_{SPP} = 2\,\mu$m due to SPP coupling within tungsten thin film only appears for TM waves. Therefore, for the multilayer emitter with alternating tungsten and alumina layers, the bottom tungsten layer contributes most of the thermal emission to the cell, and the SPP coupling in tungsten thin film spectrally enhances the radiative flux.

3.4 Performance of the Near-Field TPV System at Different Vacuum Gap Distances. Calculated from the Eq. (6), the quantum efficiencies against wavelength at different vacuum gap distances are shown in Fig. 6(*a*). When the wavelength is larger than $\lambda_g = 2.22\,\mu$m, which means that the photon energy is below bandgap, no electron–hole pair is generated, so the quantum efficiency is zero. On the other hand, for smaller wavelength, most of the photons will be absorbed close to the cell surface because of small penetration depth in the near field. Thus, due to strong surface recombination, the quantum efficiency also decreases at small wavelengths. The quantum efficiency is around $\eta_q = 80\%$ within the wavelength band from 1 μm to 2 μm. Note that it has smaller quantum efficiency at 10 nm vacuum gap because of smaller penetration depths.

Integrating the spectral photocurrent density over the wavelength, the photocurrent density generated in different regions of TPV cell as a function of vacuum gap distance is obtained in Fig. 6(*b*). From this figure, most of the photocurrent is generated

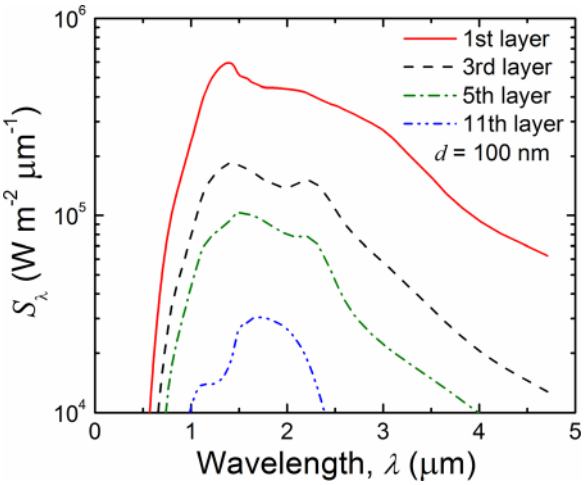

Fig. 5 The spectral heat flux emitted from different tungsten layer of the multilayer emitter. When considering the emission from a single layer, the other layers just function as the filters. The vacuum gap distance is 100 nm.

in the n-region because most of the energy is absorbed in the n-region. When the vacuum gap distance decreases, more photocurrent is generated in the p-region, because smaller gap distance means smaller penetration depth and more energy will be absorbed close to the cell surface.

The electrical power output and radiative power input of the TPV system for both multilayer emitter and plain tungsten emitter are plotted as a function of vacuum gap distance in Fig. 7(*a*). Because of the enhanced spectral heat flux with the multilayer emitter indicated in Fig. 2, the radiative power input is enhanced compared to the plain tungsten emitter. Moreover, the electrical power output is improved due to the enhanced spectral heat flux above bandgap. As shown in Fig. 7(*b*), the increase rate of radiative power input is greater than that of the electrical power output, thus, the conversion efficiency of the TPV system with the multilayer emitter is actually lower than that with a plain tungsten emitter. A higher electrical power output of about $P_E = 0.34\,\text{MW/m}^2$ and a lower conversion efficiency of $\eta = 17.2\%$ of the TPV system with the multilayer emitter are achieved at 100 nm vacuum gap.

3.5 Effects of Gold Back Reflector and ITO Front Contact for the TPV Cell. Compared with the plain tungsten emitter, the conversion efficiency is decreased using the multilayer emitter, which is due to more useless spectral radiative heat flux below the bandgap as shown in Fig. 3. In order to decrease this fraction of heat flux and thus to increase the conversion efficiency, a gold reflector on the back of n-region layer is applied to reflect the long wavelength heat flux back to the emitter. The optical properties of gold is obtained from Palik's tabular data [28]. In practice, the gold reflector also works as the back electrode to extract the photon generated free charges. Moreover, the transparent conducting oxide material ITO is considered as the front electrode to construct the TPV cell as a practical device. Here, the thickness of the ITO layer is set as 5 nm in order to minimize the light absorption by ITO. The dielectric function of ITO in near-infrared region can be simply described by a Drude model [43], while ITO is known as a low-loss plasmonic material in near IR than noble metals.

Figure 8 shows spectral heat flux incident onto the TPV cell without and with opaque gold back electrode and 5-nm-thick ITO front electrode. Note that the multilayer emitter is considered for all the cases. The spectral heat fluxes absorbed by the whole receiver at the vacuum gap distance of 100 nm are shown in Fig. 8(*a*). Comparing all the three results, the energy absorbed above the bandgap is almost the same, but the energy absorbed below the bandgap is greatly decreased with the gold reflector. This indicates that the lower radiative power input can be achieved with the same electrical power output. On the other hand, as can be seen from Fig. 8(*a*), adding a 5-nm-thick ITO layer on top of TPV cell has minimal effect on spectral heat flux with 100 nm vacuum gap. However, with a vacuum gap distance of 10 nm as shown in Fig. 8(*b*), a high spectral heat flux peak at the wavelength around $\lambda = 1.2\,\mu$m occurs by adding an ITO front layer. This is due to the SPP coupling within ITO film, and most of the energy with small

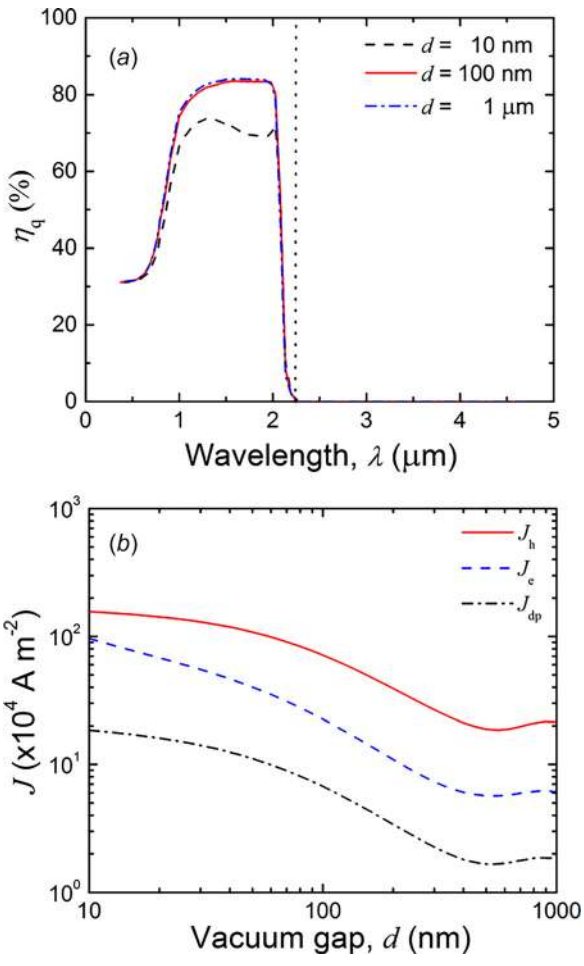

Fig. 6 (*a*) The quantum efficiency (QE) versus wavelength for different vacuum gap distances. (*b*) The photocurrent density generated in different regions of TPV cell against different vacuum gap distances.

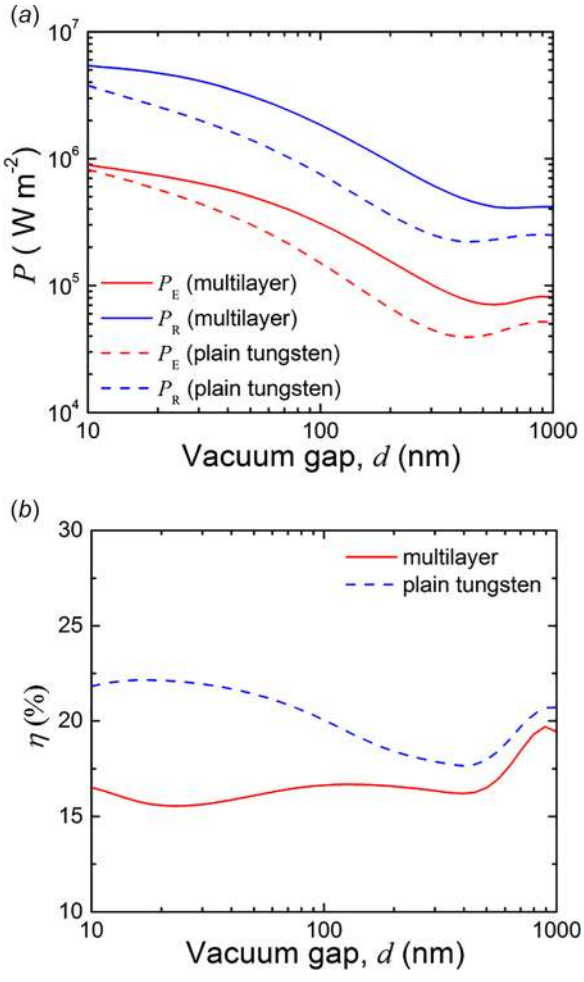

Fig. 7 (*a*) The electrical power output and radiative power input, and (*b*) the conversion efficiency of the TPV system for both multilayer emitter and plain tungsten emitter versus vacuum gap distance

penetration depth due to small vacuum gap distance will be absorbed by ITO thin film.

The radiative power input and electrical power output for all the three cases are plotted in Fig. 9(*a*). As expected from Figs. 8(*a*) and 8(*b*), a smaller radiative power input and almost the same electrical power output can be achieved when adding a gold reflector. However, different from gold reflector, adding ITO front layer will greatly increase the radiative power input at small vacuum gap distances. Because at small vacuum gap distances, the enhanced energy input is mainly absorbed in the ITO thin film, the electrical power output remains almost the same.

Finally, the conversion efficiencies with and without electrical contacts are shown in Fig. 9(*b*). Because of the decreased radiative power input, much higher conversion efficiency is achieved when using a gold reflector. At the vacuum gap of $d = 100$ nm, the conversion efficiency with the multilayer emitter is increased from $\eta = 16.6\%$ with a bare semi-infinite TPV cell to $\eta = 25.6\%$ after adding a gold reflector at the cell backside, exceeding that for plain tungsten emitter and bare TPV cell ($\eta = 20.0\%$). Therefore, both the electrical power output and conversion efficiency are improved when using the multilayer emitter and gold backside electrode for the TPV cell. In addition, when adding a 5-nm-thick ITO layer as the front electrode, a high conversion efficiency of 23.7% is still achieved at $d = 100$ nm, while conversion efficiency will decrease because of the higher radiative power input at vacuum gap distance smaller than 50 nm. Compared to the significant improvement of conversion efficiency from 16.6% to 23.7% after adding Au reflector and ITO front contact for multilayer emitter, the conversion efficiency increase for plain tungsten emitter is smaller than 2% after adding these two layers.

4 Conclusion

A multilayer emitter with alternating tungsten and alumina layer and the TPV cell of $In_{0.18}Ga_{0.82}Sb$ are applied to construct a near-field TPV system. The spectral heat flux is much enhanced by replacing the plain tungsten emitter with multilayer emitter, and the thicknesses of tungsten and alumina layer are, respectively, optimized as $t_W = 10$ nm and $t_{Al_2O_3} = 300$ nm to maximize the electrical power output for bare TPV cell at $d = 100$ nm. It is also shown that EMT fails to accurately predict the SPP coupling within the tungsten thin film, which is responsible for the spectral heat flux enhancement just above the cell bandgap. By considering the charge transport in different regions of TPV cell, the photocurrent density in different regions and the electrical power output are calculated. With an opaque gold reflector beneath the TPV cell and a 5-nm-thick ITO layer as the front contact, the conversion efficiency of $\eta = 23.7\%$ and electrical power output of $P_E = 0.31\ MW/m^2$ can be achieved at the vacuum gap of $d = 100$ nm when the emitter and receiver temperatures are set as

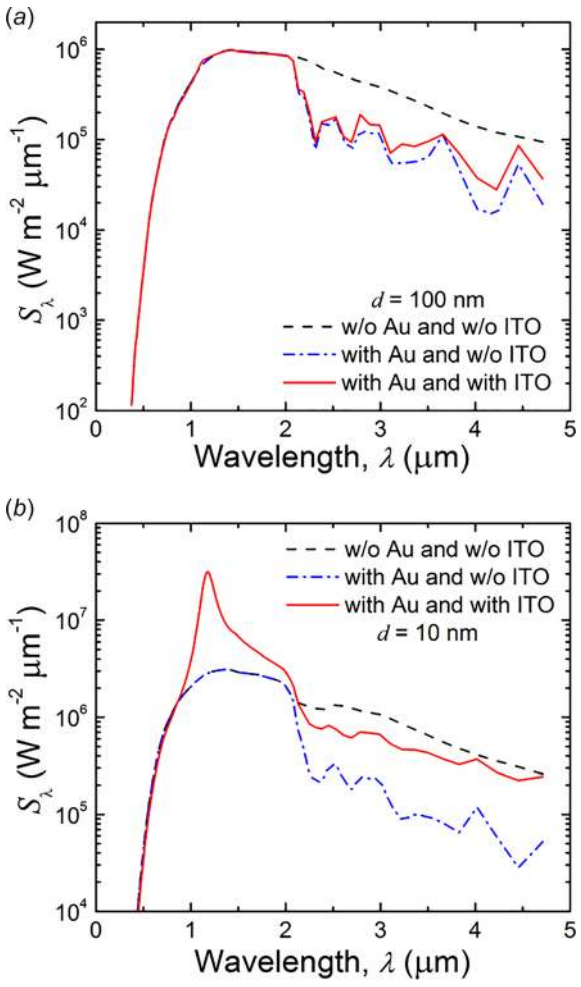

Fig. 8 (*a*) The spectral heat fluxes absorbed by the receiver versus wavelength at $d = 100$ nm and (*b*) $d = 10$ nm for three different cases, which are just semi-infinite TPV cell, TPV cell with opaque Au on the back, and TPV cell with both opaque Au on the back and 5-nm-thick ITO at the front, respectively

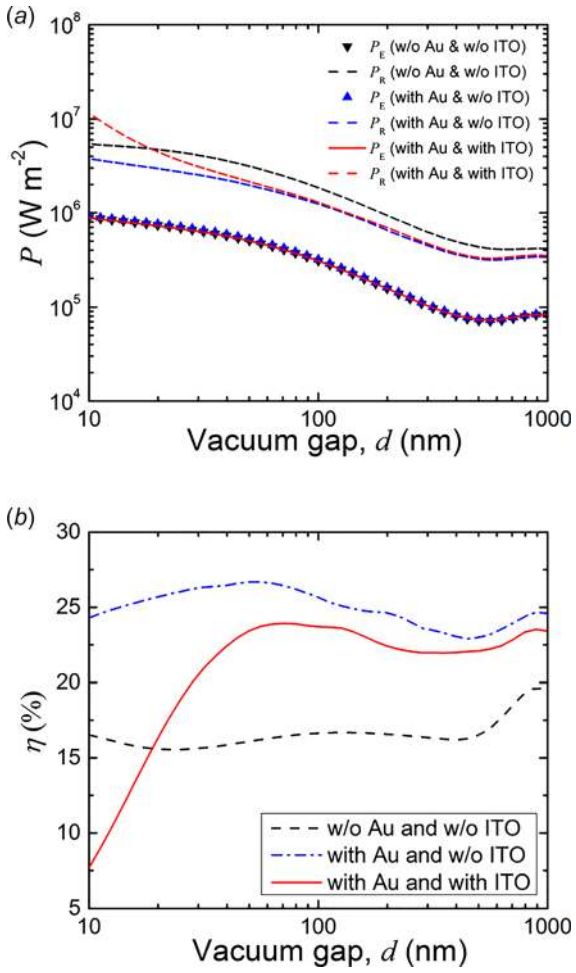

Fig. 9 (*a*) The radiative power input and electrical power output versus vacuum gap distance, and (*b*) the conversion efficiency versus vacuum gap distance for three different cases, which are just semi-infinite TPV cell, TPV cell with opaque Au on the back, and TPV cell with both opaque Au on the back and 5-nm-thick ITO at the front, respectively

$T_H = 2000$ K and $T_L = 300$ K, respectively. The results will facilitate the experimental demonstration of high-efficiency near-field TPV systems and future applications in energy conversion.

Acknowledgment

Supports from the National Science Foundation under Grant No. CBET-1454698 (YY and LW) and ASU New Faculty Startup fund (JYC) are greatly acknowledged.

Nomenclature

c_0 = light velocity in vacuum (2.997×10^8 m s^{-1})
d_l = thickness of lth layer in receiver (m)
e = charge of electron (1.6×10^{-19} C)
$\mathbf{E}$ = electric field vector (V/m)
E_g = bandgap of TPV cell (eV)
f = filling ratio of metal in multilayer structure
g = electron–hole generation rate
$\bar{\bar{\mathbf{G}}}_e$ = electric-field dyadic Green's function (m^{-1})
h = Planck constant, 6.626×10^{-34} m^2 kg s^{-1}
$\mathbf{H}$ = magnetic field vector (A/m)
$\boldsymbol{j}$ = fluctuating current density (A m^{-2})
J = drift current density (A m^{-2})
J_{ph} = short circuit current (A m^{-2})
k_z = wavevector vertical to interface
L = thickness of different region in TPV cell (m)
P_E = electrical power output (W m^{-2})
P_R = radiative power input (W m^{-2})
q'' = radiative heat flux (W m^{-2})
$Q_{\lambda,l}$ = spectral heat flux absorbed in lth layer (W m^{-2} μm^{-1})
$\mathbf{S}_\omega$ = spectral Poynting vector (W s m^{-2} rad^{-1})
$S_{z,\omega}$ = spectral heat flux in z direction (W s m^{-2} rad^{-1})
T = temperature (K)
V_{oc} = open circuit voltage (V)
$\mathbf{x}$ = space variable (m)
$\mathbf{x'}$ = space variable (m)
z_m = z position of mth layer (m)

Greek Symbols

β = wavevector parallel to the interface
ε = relative electric permittivity
ε_d = relative electric permittivity of dielectric
ε_m = relative electric permittivity of metal
λ = wavelength (m)
η = conversion efficiency
η_q = quantum efficiency
μ_0 = magnetic permeability in vacuum, $4\pi \times 10^{-7}$ N A^{-2}
ξ = energy transmission coefficient
ω = angular frequency (rad s^{-1})

Subscripts

dp = depletion region of TPV cell
e = electron in the p-region
h = hole in the n-region
$\perp$ = direction vertical to the surface
$\parallel$ = direction parallel to the surface

Superscript

* = complex conjugate

References

[1] Basu, S., Chen, Y. B., and Zhang, Z. M., 2007, "Microscale Radiation in Thermophotovoltaic Devices—A Review," Int. J. Energy Res., **31**(6), pp. 689–716.
[2] Basu, S., and Wang, L. P., 2013, "Near-Field Radiative Heat Transfer Between Doped Silicon Nanowire Arrays," Appl. Phys. Lett., **102**(5), p. 053101.
[3] Basu, S., Zhang, Z. M., and Fu, C. J., 2009, "Review of Near-Field Thermal Radiation and Its Application to Energy Conversion," Int. J. Energy Res., **33**(13), pp. 1203–1232.
[4] Shen, S., Mavrokefalos, A., Sambegoro, P., and Chen, G., 2012, "Nanoscale Thermal Radiation Between Two Gold Surfaces," Appl. Phys. Lett., **100**(23), p. 233114.
[5] Shen, S., Narayanaswamy, A., and Chen, G., 2009, "Surface Phonon Polaritons Mediated Energy Transfer Between Nanoscale Gaps," Nano Lett., **9**(8), pp. 2909–2913.
[6] Narayanaswamy, A., Shen, S., and Chen, G., 2008, "Near-Field Radiative Heat Transfer Between a Sphere and a Substrate," Phys. Rev. B, **78**(11), p. 115303.
[7] Whale, M., and Cravalho, E. G., 2002, "Modeling and Performance of Microscale Thermophotovoltaic Energy Conversion Devices," IEEE Trans. Energy Convers., **17**(1), pp. 130–142.
[8] Laroche, M., Carminati, R., and Greffet, J.-J., 2006, "Near-Field Thermophotovoltaic Energy Conversion," J. Appl. Phys., **100**(6), p. 063704.
[9] Park, K., Basu, S., King, W. P., and Zhang, Z. M., 2008, "Performance Analysis of Near-Field Thermophotovoltaic Devices Considering Absorption Distribution," J. Quant. Spectrosc. Radiat Transfer, **109**(2), pp. 305–316.
[10] Francoeur, M., Vaillon, R., and Mengüç, M. P., 2011, "Thermal Impacts on the Performance of Nanoscale-Gap Thermophotovoltaic Power Generators," IEEE Trans. Energ. Convers., **26**(2), pp. 686–698.
[11] Bright, T. J., Wang, L. P., and Zhang, Z. M., 2014, "Performance of Near-Field Thermophotovoltaic Cells Enhanced With a Backside Reflector," ASME J. Heat Transf., **136**(6), p. 062701.
[12] Chubb, D. L., and Lowe, R. A., 1993, "Thin-Film Selective Emitter," J. Appl. Phys., **74**(9), pp. 5687–5698.
[13] Chubb, D. L., and Wolford, D. S., 2005, "Dual Layer Selective Emitter," Appl. Phys. Lett., **87**(14), p. 141907.
[14] Lin, S. Y., Moreno, J., and Fleming, J. G., 2003, "Three-Dimensional Photonic-Crystal Emitter for Thermal Photovoltaic Power Generation," Appl. Phys. Lett., **83**(2), pp. 380–382.
[15] Hitoshi, S., Yoshiaki, K., and Hiroo, Y., 2005, "Tuning of the Thermal Radiation Spectrum in the Near-Infrared Region by Metallic Surface Microstructures," J. Micromech. Microeng., **15**(9), p. S243.
[16] Chen, Y. B., and Zhang, Z. M., 2007, "Design of Tungsten Complex Gratings for Thermophotovoltaic Radiators," Opt. Commun., **269**(2), pp. 411–417.
[17] Zhao, B., Wang, L. P., Shuai, Y., and Zhang, Z. M., 2013, "Thermophotovoltaic Emitters Based on a Two-Dimensional Grating/Thin-Film Nanostructure," Int. J. Heat Mass Transfer, **67**, pp. 637–645.
[18] Wang, L. P., and Zhang, Z. M., 2012, "Wavelength-Selective and Diffuse Emitter Enhanced by Magnetic Polaritons for Thermophotovoltaics," Appl. Phys. Lett., **100**(6), p. 063902.
[19] Zhao, B., and Zhang, Z. M., 2014, "Study of Magnetic Polaritons in Deep Gratings for Thermal Emission Control," J. Quant. Spectrosc. Radiat. Transfer, **135**, pp. 81–89.
[20] Molesky, S., Dewalt, C. J., and Jacob, Z., 2012, "High Temperature Epsilon-Near-Zero and Epsilon-Near-Pole Metamaterial Emitters for Thermophotovoltaics," Opt. Express, **21**(S1), pp. A96–A110.
[21] Narayanaswamy, A., and Chen, G., 2004, "Thermal Emission Control With One-Dimensional Metallodielectric Photonic Crystals," Phys. Rev. B, **70**(12), p. 125101.
[22] Narayanaswamy, A., and Chen, G., 2003, "Surface Modes for Near Field Thermophotovoltaics," Appl. Phys. Lett., **82**(20), pp. 3544–3546.
[23] Ilic, O., Jablan, M., Joannopoulos, J. D., Celanovic, I., and Soljačić, M., 2012, "Overcoming the Blackbody Limit in Plasmonic and Graphene Near-Field Thermophotovoltaic Systems," Opt. Express, **20**(S3), pp. A366–A384.
[24] Messina, R., and Ben-Abdallah, P., 2013, "Graphene-Based Photovoltaic Cells for Near-Field Thermal Energy Conversion," Sci. Rep., **3**, p. 1383.
[25] Tong, J. K., Hsu, W. C., Huang, Y., Boriskina, S. V., and Chen, G., 2015, "Thin-Film 'Thermal Well' Emitters and Absorbers for High-Efficiency Thermophotovoltaics," Sci. Rep., **5**, p. 10661.
[26] Bernardi, M. P., Dupre, O., Blandre, E., Chapuis, P. O., Vaillon, R., and Francoeur, M., 2015, "Impacts of Propagating, Frustrated and Surface Modes on Radiative, Electrical and Thermal Losses in Nanoscale-Gap Thermophotovoltaic Power Generators," Sci. Rep., **5**, p. 11626.
[27] Chang, J.-Y., Yang, Y., and Wang, L. P., 2015, "Tungsten Nanowire Based Hyperbolic Metamaterial Emitters for Near-Field Thermophotovoltaic Applications," Int. J. Heat Mass Transfer, **87**, pp. 237–247.
[28] Palik, E. D., 1998, *Handbook of Optical Constants of Solids*, Academic Press, San Diego, CA.
[29] González-Cuevas, J. A., Refaat, T. F., Abedin, M. N., and Elsayed-Ali, H. E., 2006, "Modeling of the Temperature-Dependent Spectral Response of $In_{1-x}Ga_xSb$ Infrared Photodetectors," Opt. Eng., **45**(4), p. 044001.
[30] Rytov, S. M., Kravtsov, Y. A., and Tatarskii, V. I., 1987, *Principles of Statistical Radiophysics*, Springer-Verlag, Berlin.
[31] Tsang, L., Kong, J. A., and Ding, K.-H., 2004, *Scattering of Electromagnetic Waves, Theories and Applications*, Wiley, New York.
[32] Narayanaswamy, A., and Chen, G., 2005, "Thermal Radiation in 1D Photonic Crystals," J. Quant. Spectrosc. Radiat. Transfer, **93**(1), pp. 175–183.
[33] Francoeur, M., Mengüç, M. P., and Vaillon, R., 2009, "Solution of Near-Field Thermal Radiation in One-Dimensional Layered Media Using Dyadic Green's Functions and the Scattering Matrix Method," J. Quant. Spectrosc. Radiat. Transfer, **110**(18), pp. 2002–2018.
[34] Basu, S., Wang, L. P., and Zhang, Z. M., 2011, "Direct Calculation of Energy Streamlines in Near-Field Thermal Radiation," J. Quant. Spectrosc. Radiat. Transfer, **112**(7), pp. 1149–1155.
[35] Wang, L. P., Basu, S., and Zhang, Z. M., 2011, "Direct and Indirect Methods for Calculating Thermal Emission from Layered Structures With Nonuniform Temperatures," ASME J. Heat Transfer, **133**(7), p. 072701.

[36] Cortes, C. L., Newman, W., Molesky, S., and Jacob, Z., 2012, "Quantum Nanophotonics Using Hyperbolic Metamaterials," J. Opt., **14**(6), p. 063001.
[37] Tschikin, M., Biehs, S. A., Messina, R., and Ben-Abdallah, P., 2013, "On the Limits of the Effective Description of Hyperbolic Materials in the Presence of Surface Waves," J. Opt., **15**(10), p. 105101.
[38] Yang, Y., Basu, S., and Wang, L. P., 2013, "Radiation-Based Near-Field Thermal Rectification With Phase Transition Materials," Appl. Phys. Lett., **103**(16), p. 163101.
[39] Zhu, P., Jin, P., and Guo, L. J., 2013, "Insight of Limitations of Effective Media Theory for Metal-Dielectric Multilayer Metamaterials," Opt. Commun., **305**, pp. 8–12.
[40] Liu, X. L., Bright, T. J., and Zhang, Z. M., 2014, "Application Conditions of Effective Medium Theory in Near-Field Radiative Heat Transfer Between Multilayered Metamaterials," ASME J. Heat Transfer, **136**(9), p. 092703.
[41] Liu, X. L., Zhang, R. Z., and Zhang, Z. M., 2013, "Near-Field Thermal Radiation Between Hyperbolic Metamaterials: Graphite and Carbon Nanotubes," Appl. Phys. Lett., **103**(21), p. 213102.
[42] Zhang, Z. M., 2007, *Nano/Microscale Heat Transfer*, McGraw-Hill, New York.
[43] Rhodes, C., Cerruti, M., Efremenko, A., Losego, M., Aspnes, D. E., Maria, J. P., and Franzen, S., 2008, "Dependence of Plasmon Polaritons on the Thickness of Indium Tin Oxide Thin Films," J. Appl. Phys., **103**(9), p. 093108.